The Fourth IEEE RAS/EMBS International Conference
on Biomedical Robotics and Biomechatronics
Roma, Italy. June 24-27, 2012

Wireless Magnetic-Based Control of Paramagnetic Microparticles

Islam S. M. Khalil, Jasper D. Keuning, Leon Abelmann and Sarthak Misra

Abstract— **This work investigates modeling and control of microparticles that could be guided inside the human body using external magnetic fields. Proposed areas of applications for these microparticles include but not limited to minimally invasive surgeries, diagnosis and sensing. The problem is formulated by modeling a magnetic prototype system which has been developed for the purpose of wireless motion control of microparticles. A control system is devised based on the way-point approach to control the navigation of the microparticles in a fluid. In addition, a path planning procedure based on a combination of the potential field and the A^* approaches is investigated in order to control the motion of the microparticles in the presence of static and dynamic obstacles. The experimental verification is conducted on a magnetic system designed for manipulation of microparticles. The experimental results demonstrates the motion control of microparticles with maximum steady state position tracking error of 8.6 μm within a 2.4 mm$\times$1.8 mm workspace.**

I. INTRODUCTION

Recently, there has been a growing demand for less invasive and non-surgical approaches for medical interventions and diagnosis. Microparticles that are able to be controlled inside human blood vessels could be used to carry out limited minimally invasive surgeries such as delivering highly localized pharmaceutical agents to difficult-to-access regions within the human body [1], [2]. Therefore, we developed a magnetic prototype system for controlling microparticles through externally applied magnetic fields. The developed prototype system is shown in Fig. 1, illustrating a circular trajectory tracking under the influence of controlled magnetic fields. Such magnetically-guided microparticles could be coated with concentrated drugs and steered towards diseased difficult-to-reach regions [3]. Magnetic labeling of a pharmaceutical dosage can be achieved by the incorporation of small amounts of remanent ferromagnetic particles and their subsequent magnetization. After the ingestion of a magnetically-labeled pharmaceutical capsule, the magnetic field outside the patient is measured, then the position of the capsule is determined by solving an inverse problem [4]. We consider the control of spherical microparticles, where spherical shapes simplify the control problem since there is no preferred direction of magnetization [5].

Much effort has been expended to provide microrobots with relatively miniaturized sizes in order to make them applicable for wide range of medical applications. Kummer *et al.* [6], presented a 5-DOF wireless magnetic system for controlling an untethered microrobot within a large workspace for delicate retinal applications. This wireless control was accomplished through the utilization of complex non-uniform magnetic fields. However, the size of the fabricated microrobot was relatively large (0.5 mm to 2 mm long). Nevertheless, the size of the robot was suitable for the intended application. This could possibly limit its operating range since the large arteries of the human blood circulatory system have diameters which range from 1.0 mm to 4.0 mm and from 6.0 μm to 10 μm for capillaries [7], [8]. Similarly, magnetic propulsion was utilized to move a 3 mm ferromagnetic thermoseed to reach a brain tumour [9]. Propulsion is accomplished by applying magnetic forces generated by a Magnetic Stereotaxis System which consists of six superconducting coils and a fluoroscopic imaging system [10], [11]. Additional thrust force to steer a cylindrical microrobot was achieved by embedding a spiral-shaped object. In this case, the microrobot rotates in a rotational magnetic field and the spiral shape produces additional thrust force [12].

The previous attempts have limited operating range due to the size of their microrobots. The smaller the microrobot (e.g., thermoseed or a spiral-shaped object) is, the wider its operating range becomes. In this sense, microparticles have an advantage due to their miniature size.

The exact mapping between the force acting on a microparticle and the applied weak magnetic fields (i.e., less than 3 mT) was derived in [13]. This mapping modifies

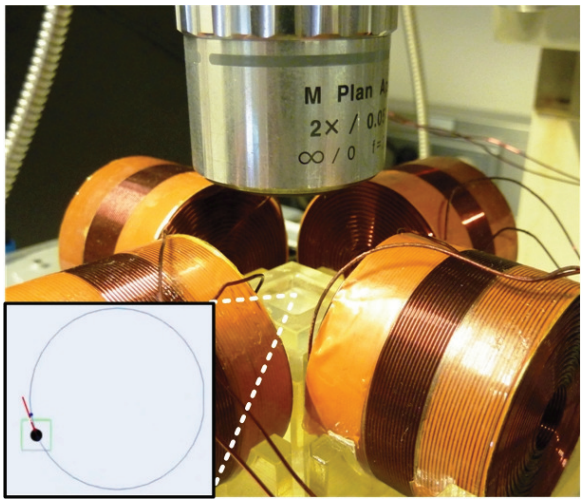

Fig. 1. The magnetic prototype system developed for the wireless control of microparticles. The inset shows a 100 μm spherical microparticle in a water reservoir tracking a circular trajectory by the controlled magnetic fields generated at the electromagnets.

Islam S. M. Khalil, Jasper D. Keuning and Sarthak Misra are with MIRA–Institute for Biomedical Technology and Technical Medicine, University of Twente, The Netherlands i.s.m.khalil@utwente.nl

Leon Abelmann is with MESA+ Institute for Nanotechnology, University of Twente, The Netherlands

the conventional expression of the force experienced by a microparticle, by accounting for the non-zero initial magnetization, which may contribute significantly to the force under the influence of weak magnetic field.

In this work, we discuss the modeling and control of microparticles, using a magnetic prototype system which has been developed in our laboratory for manipulation applications [14]. Weak magnetic fields are generated using air-core electromagnets. In this case, the magnetic field can be determined by the superposition of each electromagnet contribution during the computation of the magnetic force experienced by the microparticles. A finite element (FE) model of the system is developed and verified experimentally in order to determine the current-field map. Position of the microparticle is measured using a vision system and utilized in the realization of the force-magnetic field (or force-current) map. In addition, navigation of the microparticle is controlled in the presence of static and dynamic virtual obstacles using a combination of the potential field and the A^* approaches [15]-[16].

The remainder of this paper is organized as follows: In Section II, we shall discuss the theoretical background pertaining to the general modeling and control of microparticles under the influence of external magnetic fields. In addition, a FE model is developed to analyze the force-current map of the magnetic system. Motion control of the microparticle using the waypoint approach is provided in Section III. Description of the magnetic system along with the procedure of implementation and experimental results are included in Section IV. Finally, Section V provides conclusions and final remarks.

II. Magnetic Force Modeling

The magnetic force ($\mathbf{F}(\mathbf{P}) \in \mathbb{R}^{3\times 1}$) acting on a magnetic dipole (small body) is given by

$$\mathbf{F}(\mathbf{P}) = \nabla(\mathbf{m}(\mathbf{P}) \cdot \mathbf{B}(\mathbf{P})), \tag{1}$$

where $\mathbf{m}(\mathbf{P}) \in \mathbb{R}^{3\times 1}$ and $\mathbf{B}(\mathbf{P}) \in \mathbb{R}^{3\times 1}$ are the permanent or induced magnetic dipole moment of the microparticle and the induced magnetic field at a point ($\mathbf{P} \in \mathbb{R}^{3\times 1}$), respectively. The microparticles we consider in this work are spherical and have negligible intrinsic anisotropy. As a result, they are superparamagnetic at room temperature. Therefore, we can approximate the magnetic dipole ($\mathbf{m}(\mathbf{P})$) with

$$\mathbf{m}(\mathbf{P}) = \frac{4}{3}\pi r_p^3 \frac{\chi_m}{\mu_0(1+\chi_m)}\mathbf{B}(\mathbf{P}), \tag{2}$$

where r_p is the radius of the spherical microparticle. Further, χ_m and μ_0 are the magnetic susceptability constant and the vacuum permeability (i.e., $\mu_0 = 4\pi \times 10^{-7}$T.m/A), respectively [9]. Substitution of (2) in (1) yields

$$\mathbf{F}(\mathbf{P}) = \frac{4}{3}\frac{1}{\mu}\pi r_p^3 \chi_m \nabla(\mathbf{B}^2(\mathbf{P})), \tag{3}$$

where $\mu = \mu_0(1+\chi_m)$, is the permeability coefficient.

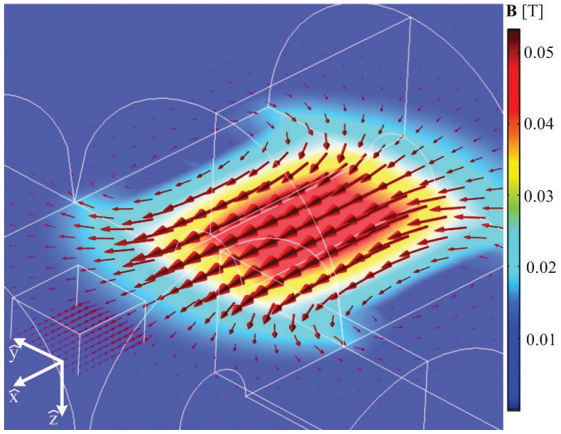

Fig. 2. Finite element simulation of a single electromagnet for current input of 0.8 A. The planar magnetic fields are only shown in the figure due to their symmetric pattern with respect to the axis of the cylindrical electromagnet. Theoretically, the constant matrix $\widetilde{\mathbf{B}}_i(\mathbf{P})$ can be determined using this analysis. Manipulation of the microparticles occurs in the xy-plane which coincides with the center plane of the electromagnets. The FE model is created using Comsol Multiphysics® (COMSOL, Inc., Burlington, U.S.A).

Since the magnetic field is generated using air-core electromagnets, the magnetic field can be determined by the superposition of the contribution of each of the electromagnets

$$\mathbf{B}(\mathbf{P}) = \sum_{i=1}^{n} \mathbf{B}_i(\mathbf{P}), \tag{4}$$

where n is the number of electromagnets within the magnetic system. The magnetic field ($\mathbf{B}_i(\mathbf{P})$) due to each electromagnet is linearly proportional to the applied current (I_i) at each electromagnet. Therefore, (4) can be rewritten as

$$\mathbf{B}(\mathbf{P}) = \sum_{i=1}^{n} \widetilde{\mathbf{B}}_i(\mathbf{P}) I_i = \widetilde{\mathbf{B}}(\mathbf{P})\mathbf{I}, \tag{5}$$

where $\widetilde{\mathbf{B}}(\mathbf{P}) \in \mathbb{R}^{3\times n}$ is a matrix which depends on the position at which the magnetic field is measured and $\mathbf{I} \in \mathbb{R}^{n\times 1}$ is a vector of the applied current [6]. The magnetic field due to each electromagnet is related to the current input by $\widetilde{\mathbf{B}}_i(\mathbf{P})$. We can determine $\widetilde{\mathbf{B}}(\mathbf{P})$ experimentally by measuring the magnetic field at every point within the workspace of the system. Alternatively, $\widetilde{\mathbf{B}}(\mathbf{P})$ can be determined by creating a field map using FE analysis.

The FE analysis of the current-field map is illustrated in Fig. 2. This map has to be constructed for each electromagnet. Then due to its linearity, the matrix $\widetilde{\mathbf{B}}(\mathbf{P})$ can be determined by the superposition of each electromagnet contribution. Results of the FE analysis are shown in Fig. 3. The magnetic field components (B_x and B_y) are illustrated in Figs. 3(a) and (b), respectively. A 5th order polynomial yielded minimum sum squares for error with the following coefficients for B_x: [0.0 0.0 0.3 $-$ 9.0 0.0 18.0 5.7 $-$ 1141.0 0.0 758.9 1.1×10^4 394.7 -7.9×10^4 -531.4 2.6×10^4 $-$ 8.8×10^4 1.5×10^4 $-$ 1.4×10^5 $-$ 3.6×10^6 $-$ 3.5×10^4 5.8×10^5], and the following coefficients for B_y: [-1.2×10^{-6} -0.1 0.0 0.0 -18.0 0.0 286.1 2.2 -1125.0 $-$

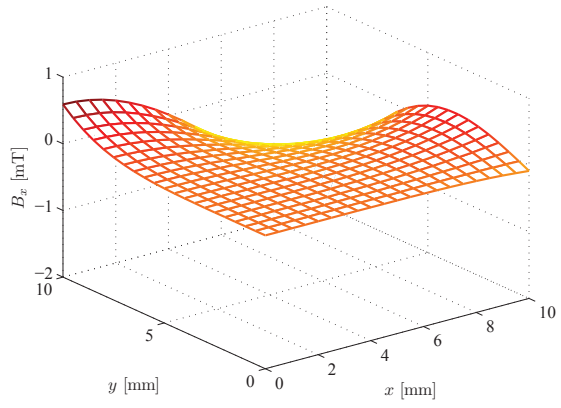

(a) Magnetic field component B_x

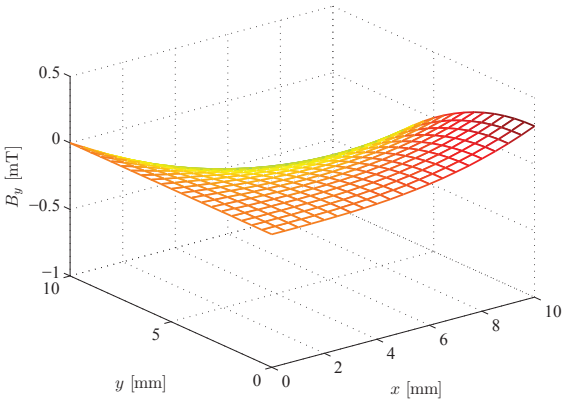

(b) Magnetic field component B_y

Fig. 3. Results of the FE analysis for the field components of a single air-core electromagnet when current of 0.8 A is applied. We obtained a 5th order polynomial which yielded minimum sum of squares for error. The results of the FE analysis are utilized during the computation of the gradient $\nabla(\mathbf{B}^2(\mathbf{P}))$ which is used in the realization of the force-current map (9).

$0.7\ -45.7\ 4.0\times10^4\ 41.0\ -5.2\times10^4\ 529.3\ -3.5\times10^5\ 4.8\times 10^4\ 2.8\times10^6\ -7.9\times10^4\ -1.9\times10^6\ 4.6\times10^4]$. The magnetic field component in z-direction is zero (i.e., $B_z = 0$), since we are only considering planar motion control of the microparticles in xy-plane at $z = 0$. This is also considered during the design of the magnetic prototype system, as the plane at which the manipulation occurs must be collinear with the center plane of the electromagnets as shown in Fig. 4.

With respect to a basis of orthogonal vectors (i.e., $\widehat{\mathbf{x}}$, $\widehat{\mathbf{y}}$ and $\widehat{\mathbf{z}}$) that are shown in Fig. 2, the magnetic field can be expressed as

$$\mathbf{B}(\mathbf{P}) = B_x\widehat{\mathbf{x}} + B_y\widehat{\mathbf{y}} + B_z\widehat{\mathbf{z}}. \tag{6}$$

Therefore, $\nabla(\mathbf{B}^2(\mathbf{P}))$ can be computed using the magnetic field gradient as follows:

$$\begin{aligned}\nabla(\mathbf{B}^2(\mathbf{P})) &= \nabla(B_x^2 + B_y^2 + B_z^2) = \nabla(\Omega) \\ &= \frac{\partial\Omega}{\partial x}\widehat{\mathbf{x}} + \frac{\partial\Omega}{\partial y}\widehat{\mathbf{y}} + \frac{\partial\Omega}{\partial z}\widehat{\mathbf{z}},\end{aligned} \tag{7}$$

where Ω is a scalar function

$$\Omega = B_x^2 + B_y^2 + B_z^2.$$

It is important to note that stable equilibrium at any point in the system's workspace, perhaps at $z = 0$ ($\mathbf{P}_{z=0}$ represents a point located on the horizontal xy-plane shown in Fig. 2), cannot be achieved without feedback control. This can be shown using (3). For $\mathbf{P}_{z=0}$ to be a stable equilibrium point, the divergence of the force field must be negative, i.e., $\nabla\cdot\mathbf{F}(\mathbf{P}_{z=0}) < 0$. Using (3), we obtain

$$\nabla\cdot\big[\frac{4}{3}\frac{1}{\mu}\pi r_p^3\chi_m\nabla(\mathbf{B}^2(\mathbf{P}))\big] < 0. \tag{8}$$

The scalar result of the divergence operator (8) has to be negative, which is a necessary condition for $\mathbf{P}_{z=0}$ to be a stable equilibrium point [9]. Here the divergence of the gradient of $\mathbf{B}^2(\mathbf{P})$ is positive everywhere (and so do the other parameters, except the susceptibility χ_m). Paramagnetic materials have positive susceptibility unlike diamagnetic materials [20]. Therefore, stable equilibrium cannot be achieved under static force field, it can be rather achieved by applying feedback-based control inputs. Substituting (5) in (3) yields

$$\mathbf{F}(\mathbf{P}) = \frac{4}{3}\frac{1}{\mu}\pi r_p^3\chi_m\mathbf{I}^{\mathrm{T}}\big(\nabla(\widetilde{\mathbf{B}}^{\mathrm{T}}(\mathbf{P})\widetilde{\mathbf{B}}(\mathbf{P}))\big)\mathbf{I}, \tag{9}$$

and the components ($\mathrm{F}_l(\mathbf{P})$) of the magnetic force ($\mathbf{F}(\mathbf{P})$) are given by

$$\mathrm{F}_l(\mathbf{P}) = \frac{4}{3\mu}\pi r_p^3\chi_m\mathbf{I}^{\mathrm{T}}\big(\frac{\partial(\widetilde{\mathbf{B}}^{\mathrm{T}}(\mathbf{P})\widetilde{\mathbf{B}}(\mathbf{P}))}{\partial l}\big)\mathbf{I} \text{ for } (l = x, y, z).$$

Therefore, controlling the currents at each electromagnet will allow us to impose different force vectors on the microparticle. However, in order to impose desired forces, we have to solve (9) for the currents at each electromagnet of the system. In order to determine the current vector ($\mathbf{I}\in\mathbb{R}^{n\times1}$), we have to solve the quadratic matrix equation (9) for $\mathbf{I}$ (the magnetic force is linear with respect to the current squared).

It is important to note that the force-current map (9) requires computation of the gradient $\nabla(\widetilde{\mathbf{B}}^{\mathrm{T}}(\mathbf{P})\widetilde{\mathbf{B}}(\mathbf{P}))$ at every point of the magnetic system's workspace. Based on the position of the microparticle within the workspace, the force-current map can be evaluated.

It can be shown from (9) that the generated force is a function of the microparticle size and geometry. In addition, the magnitude of the magnetic force can be increased by generating large directional derivatives in the applied field. During the initial steps of the magnetic system design, the force-current map (9) is used to determine whether the generated magnetic force would overcome the viscous drag force (F_d) generated due to the presence of the microparticle inside a fluid with known parameters. Therefore, it is important to determine the forces acting on the microparticles. First, we have to determine Reynolds number (R_e) of the fluid [14]

$$R_e = \frac{2\rho_f v r_p}{\eta}, \tag{10}$$

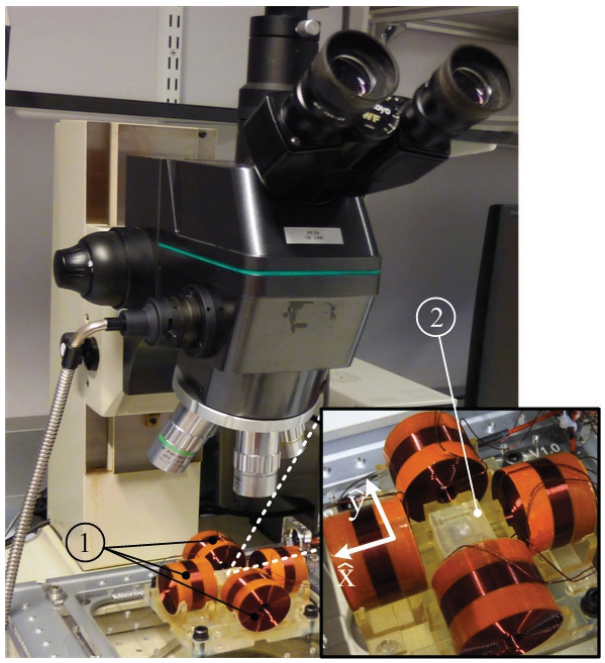

Fig. 4. The magnetic prototype system consists of a microscope with a vision system mounted on the top of an array of electromagnets ① surrounding a reservoir ② which contains water. The manipulation plane at the reservoir coincides with the center plane of the electromagnets [14]. The inset shows the water reservoir and the electromagnets array. The microparticles utilized throughout the experimental work are paramagnetic with saturation magnetization of 6.6×10^{-3} $\mathrm{Am^2/g}$, consisting of iron-oxide in a poly (lactic acid) matrix (PLAParticles-M-redF-plain from Micromod Partikeltechnologie GmbH, Rostock-Warnemuende, Germany).

where v, η and ρ_f are the microparticle velocity, fluid dynamic viscosity (1 $\mathrm{mPa.s}$) and density (998.2 $\mathrm{kg/m^3}$), respectively. Assuming that v will not exceed 1 mm/s, Reynolds number turned out to be less than 0.1. Therefore, we can assume laminar flow condition and use Stokes law

$$\mathrm{F}_d = 6\pi\eta r_p v. \tag{11}$$

In addition, the net buoyancy force (necessary when microparticle is required to navigate in three-dimensional space) acting on the microparticle is

$$\mathrm{F}_b = V(\rho_b - \rho_f)g, \tag{12}$$

where V and ρ_b are the volume ($r_p = 50$ μm) and density ($1.4{\times}10^3$ $\mathrm{kg/m^3}$) of the microparticle, respectively. Further, g is the acceleration due to gravity [21]. The net drag force is used during the design of the magnetic system such that the maximum force (i.e., 0.91 nN which can be generated by a field gradient ($\nabla(\mathbf{B^2(P)})$) of 15 $\mathrm{mT^2/m}$ in the center of the reservoir) obtained through (9) is larger than the maximum net drag force (i.e. 0.28 nN for microparticle velocity of 300 $\mu\mathrm{m/s}$). The generated magnetic force has to be applied such that the microparticle follows a reference trajectory in order to reach to a target position along with avoiding any static or dynamic obstacles along its path.

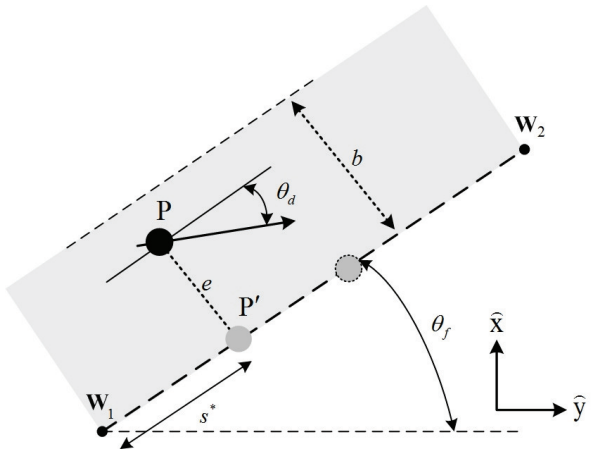

Fig. 5. The transition region around a line segment of the reference trajectory. Waypoints ($\mathbf{W}_1$ and $\mathbf{W}_2$) are defined along the reference trajectory, the line segment between the waypoints has an angle (θ_f) with the global reference frame. The width of the transition region is defined by b, the velocity vector of the microparticle has an angle (θ_d) with respect to the segment of the reference trajectory. The projection of the microparticle position ($\mathbf{P}'$) is located at s^* along the trajectory. The magnitude of the position tracking error (e) determines the type of control to be applied as it indicates whether the microparticle is located inside or outside the transition region.

III. Microparticle Motion Control

In order to control the motion of the microparticle, we define a transition region around the reference trajectory indicated by dashed lines which lies at a distance (b) on each side of the trajectory as shown in Fig. 5. Different motion control inputs are applied depending on the position of the microparticle with respect to the transition region boundaries, namely the outside and inside the transition region control inputs. Outside the transition region, the control system is designed such that the magnetic force enforces the microparticle to move towards the region boundary in finite time. Hereafter, another control input is utilized in order to achieve smooth transient response inside the transition region. We define $\mathbf{W_1}$ and $\mathbf{W_2}$ as the waypoints along the reference trajectory. The microparticle should move towards the second waypoint ($\mathbf{W_2}$). Using the cartesian components of the waypoints, we can determine the angle (θ_f) of a line segment along the trajectory with respect to the global coordinate frame shown in Fig. 5

$$\theta_f = \mathrm{atan2}(w_{2x} - w_{1x}, w_{2y} - w_{1y}), \tag{13}$$

where w_{1x} and w_{1y}, w_{2x} and w_{2y} are the components of $\mathbf{W_1}$ and $\mathbf{W_2}$, respectively. Position of the microparticle along the trajectory is

$$s^* = \frac{(\mathbf{P} - \mathbf{W_1})^{\mathrm{T}}(\mathbf{W_2} - \mathbf{W_1})}{\parallel \mathbf{W_2} - \mathbf{W_1} \parallel^2}, \tag{14}$$

which is used in the determination of the position tracking error (e) through

$$e = \parallel \mathbf{P} - (s^*(\mathbf{W_2} - \mathbf{W_1}) + \mathbf{W_1}) \parallel . \tag{15}$$

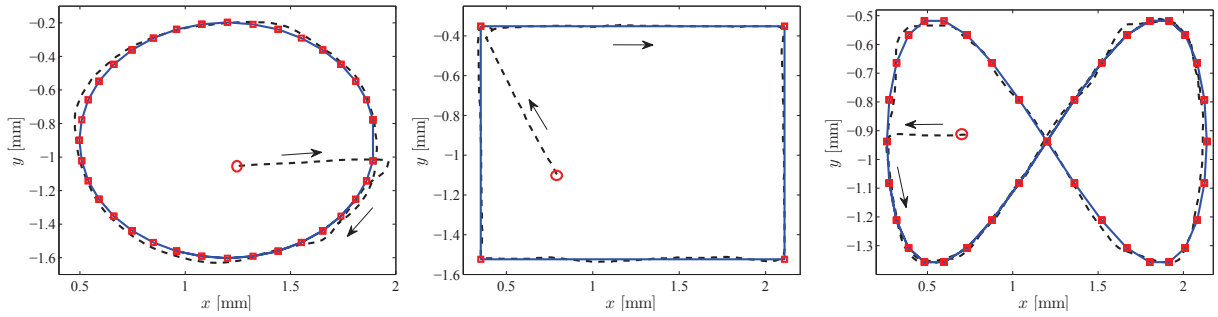

(a) Tracking a circular path (b) Tracking a rectangular path (c) Tracking a figure-eight path

Fig. 6. Experimental motion control results of the microparticle during tracking of circular, rectangular and figure-eight paths. The blue trajectory represents the reference path and the waypoints along this path are illustrated with the red squares. The black dashed-line represents the actual path taken by the microparticle. The red circle indicates the initial position of the microparticle. Controller gains are: (a) $k_p = 2.07$, $k_i = 1.00$, $b = 300$ μm and $\theta_d = \frac{\pi}{2}$. (b) $k_p = 1.00$, $k_i = 1.00$, $b = 300$ μm and $\theta_d = \frac{\pi}{2}$. (c) $k_p = 1.44$, $k_i = 1.00$, $b = 300$ μm and $\theta_d = \frac{\pi}{2}$. *Please refer to the attached video that demonstrates the results of the motion control experiments.*

The side of the trajectory at which the microparticle is located, can be distinguished by the sign of a variable σ using

$$\sigma = \text{sgn}[(\mathbf{W_2} - \mathbf{W_1}) \times (\mathbf{P} - \mathbf{W_1})]. \quad (16)$$

We assume that the reference trajectory consists of a set of waypoints connected by straight lines. Switching between waypoints depends on the value of s^*, i.e., the microparticle passes the second waypoint if $s^* > 1$. Hereafter, we have to switch to the next waypoint and so forth. On the other hand, the value of $\mid e \mid$ determines the nature of the applied control input as it indicates whether the microparticle is located outside ($\mid e \mid > b$) or inside ($\mid e \mid \leq b$) the transition region.

A. Outside the transition region

Considering that the microparticle is navigating outside the transition region, i.e., $\mid e \mid > b$, the applied magnetic force has to enforce the microparticle towards the transition region. This can be achieved if the applied magnetic force vector enforced the microparticle to move with an angle (θ_c) with respect to the global coordinate frame shown in Fig. 5

$$\theta_c = \theta_f - \sigma\theta_d, \quad (17)$$

where $\theta_d \in (0, \frac{\pi}{2})$ is the entry heading angle of the microparticle. It was proved in [22], that the previous control input (17) enforces the microparticle to entre the transition region in finite time. Determination of the right hand side of (17) requires measuring the position components of the microparticle along with the components of the waypoints (w_{1x} and w_{1y}, w_{2x} and w_{2y}). Afterwards, the force-current map (9) derived in Section II can be used in order to determine the desired current for each of the electromagnets.

B. Inside the transition region

Considering that the microparticle is navigating inside the transition region, i.e., $\mid e \mid \leq b$, the applied magnetic force has to enforce the microparticle to move with an angle

$$\theta_c = \frac{e}{|e|}\frac{\pi}{2}\left(\frac{|e|}{b}\right)^{k_p} + k_i \int_0^t e\text{d}t, \quad (18)$$

with respect to the global coordinate frame, where k_p and k_i are the controller gains which have to be selected upon the desired transient response. It is worth noting that the controller gains are not limited to k_p and k_i. The heading angle (θ_d) and the boundary width (b) can be tuned in order to achieve the desired tracking performance. Increasing k_p and $\theta_d \in (0, \frac{\pi}{2})$ results in faster response and shorter convergence time to the desired trajectory, whereas k_i reduces the tracking error in the steady state.

IV. Magnetic System Design and Results

The proposed magnetic prototype system consists of air-core electromagnets, vision system and control system. Using the FE analysis, we concluded that four electromagnets (each has an inner diameter, an outer diameter and length of 10 mm, 39 mm and 30 mm, respectively. The number of turns in each coil is 1680) are enough to steer the microparticles in a planar workspace and overcome the net force resulted from the viscous fluid drag given by (11). The air-core electromagnets guarantee the validity of (5). The proposed system is illustrated in Fig. 4. The electromagnets are oriented around a reservoir containing water at which the microparticle navigates under the influence of the magnetic fields. A detailed description of the system components and specifications can be found in [14].

In order to analyze the overall system, we generated a FE model. The electromagnetic field throughout the system's workspace is determined by applying current at the coils with maximum limit of 0.8 A. The generated magnetic fields at the workspace are able to create enough magnetic force to overcome the net drag force acting on the microparticle inside the reservoir.

We have shown that feedback control must be applied in order to stabilize the microparticle since the divergence of the force field is positive according to (8). Visual feedback is used to close the control loop of the system. The desired force is determined based on the target coordinates and the obstacle-free trajectories. Afterwards, the force-current map

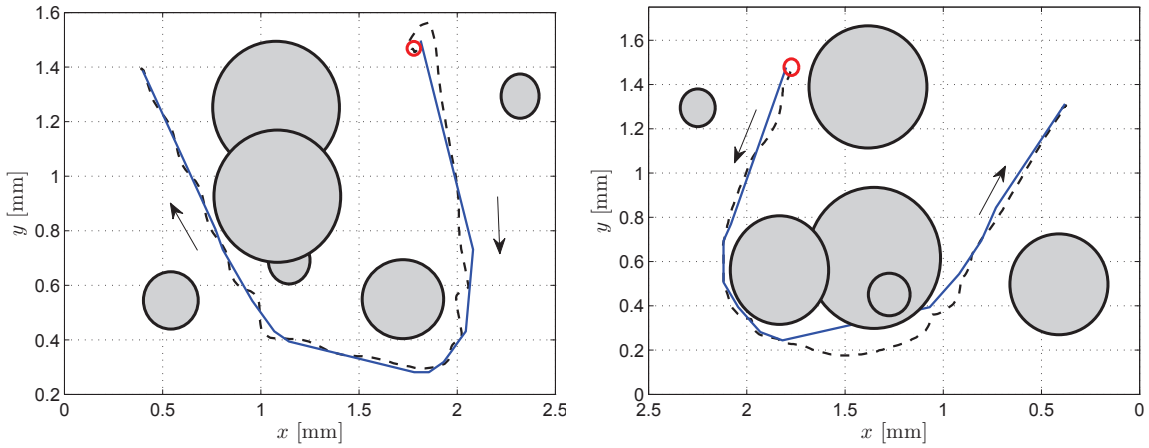

(a) Tracking in the presence of static obstacles

(b) Tracking in the presence of dynamic obstacles

Fig. 7. Motion control experimental results of the wireless magnetic control of a microparticle. A target point is tracked in the presence of static and dynamic obstacles. The gray circles represent obstacles which are avoided by utilizing a combination of the potential field and the A^* approaches to generate a feasible path. The black dashed-line represents the actual path taken by the microparticle and the blue line represents the determined obstacle-free path. (a) Static obstacle avoidance. The controller gains are: $k_p = 0.83$, $k_i = 0.58$, $b = 300$ μm and $\theta_d = \frac{\pi}{2}$. (b) Dynamic obstacle avoidance. One of the obstacles moved towards the planned path, the repulsive force field of the obstacle allowed the microparticle to avoid collision. The controller gains are: $k_p = 1.00$, $k_i = 1.00$, $b = 300$ μm and $\theta_d = \frac{\pi}{2}$. *Please refer to the attached video that demonstrates the results of the obstacle avoidance experiments*.

is used to determine the current at each electromagnet of the system by solving the quadratic matrix equation (9).

The described waypoint control approach is implemented to track the different trajectories shown in Fig. 6. These trajectories span the entire workspace of the system (i.e., 2.4 mm$\times$1.8 mm). Therefore, we can examine the control authority of the applied magnetic force throughout the entire workspace. Figs. 6(a), (b) and (c) illustrate the experimental tracking of circular, rectangular and figure-eight trajectories, respectively. In each of these experiments, four control variables (i.e., k_p, k_i, b and θ_d) can be adjusted to achieve the required transient and steady state performances. The average velocity of the microparticle depends on the shape of the reference trajectory. During the tracking of the circular, rectangular and figure-eight trajectories, the average velocity of the microparticle was 286 μm/s, 83 μm/s and 122 μm/s, respectively. The average speed difference is not only due to the different controller gains utilized in each experiment, but also due to the magnitude of the directional derivative along each path. The derivative action is not included in the control law despite of its importance because of the limited camera frame-per-second rate (i.e., 10 fps). The experimental results depicted in Fig. 6 indicate that the microparticle is controllable throughout the entire workspace (reservoir area) and the controller achieved maximum steady state position tracking error of 8.6 μm (maximum steady state position tracking error along x- and y-axis are 5.0 μm and 7.0 μm, respectively). *The attached video demonstrates our experimental results*.

In order to avoid collision with any obstacle along the path of the microparticle, we devise to combine the potential field and the A^* approaches to generate paths which avoid both static and dynamic obstacles [17], [18]. Visual feedback is utilized to determine any possible obstacle within the reservoir. This information is used in generating a path which avoids both static and dynamic obstacles. The experimental results are illustrated in Fig. 7. Experimentally, we generated virtual static and dynamic obstacles, then their coordinates are used in the realization of the obstacle-free paths. In this experiment, we utilized the potential field approach along with the A^* algorithm [15]. This is accomplished by exerting repulsive force field on the microparticle from each detected obstacle, whereas the target exerted attractive force field to pull the microparticle in its direction. Along with this approach, we utilized the A^* algorithm to find a minimal cost route towards the target. In situations at which calculations are too intensive or cannot be realized in real-time, we devise to use a combination of these two approaches by using the calculated path as a guide then using the potential field to avoid any obstacle along this path. Through this combination, we can avoid the drawbacks of each approach. In situations at which the microparticle is away from the obstacles and the target, feasible paths are generated by the A^* algorithm and if the microparticle became closer to either an obstacle or the target, the control system switches to the potential field approach and so forth.

The experimental results of the motion control in the presence of static and dynamic obstacles are illustrated in Figs. 7(a) and (b), respectively. The obstacles shown in Fig. 7 are assigned a repulsive force field while the target is assigned attractive force field. As shown in Fig. 7(b), the dynamic obstacle moved towards the planned path determined using the A^* algorithm, but due to the local repulsive force field assigned to the obstacle, the microparticle moved away from the planned path avoiding possible collision with the dynamic obstacle. *The attached video demonstrates our*

experimental results. Regardless to the simplicity of the techniques utilized in this experiment, we demonstrated the feasibility of controlling microparticles in the presence of static and dynamic obstacles by the applied magnetic fields.

V. Conclusions And Future Work

This work presented a wireless magnetic system to control the motion of paramagnetic microparticles in a fluidic body. The system is designed such that the generated magnetic force (i.e., 0.91 nN due to maximum field gradient) utilized to steer the microparticles is larger than the net viscous drag force (i.e., 0.28 nN computed at maximum microparticle velocity of 300 $\mu\mathrm{m/s}$). In view of the utilized magnetic field (less than 5 mT and maximum field gradient of 15 $\mathrm{mT^2/m}$ within the center of the workspace) and the limited frame-per-second rate (i.e., 10 fps) provided by the magnetic system and the vision system, respectively, closed-loop motion control is achieved and reference trajectories with different geometries are tracked with a maximum steady state position tracking error of 8.6 μm.

The waypoint control approach utilized in this work provides four control variables to be tuned in order to shorten the settling time and to achieve the desired transient response. In addition, a combination of the potential field and the A^* approaches is used to generate obstacle-free trajectories for the microparticle. This allows the microparticle to navigate while avoiding collision with static and dynamic obstacles.

The size of the microparticles provides them with wide range of medical applications, this is not the case when microrobot size is relatively large. However, due to the dependence of the magnetic force on the size and geometry, the magnetic force experienced by the microparticles can only be increased by generating larger directional derivatives in the applied field.

Future work in the field of wireless magnetic-based control of microparticles should be extended to investigate the control of biodegradable magnetic nanoparticles. These particles can be utilized as magnetic drug carriers owing to their low toxicity and excellent magnetic saturation. *In vivo* experiments would improve the control system design since many aspects such as time-varying fluid viscosity and flow could be investigated. In addition, the magnetic system will be re-designed to allow nano and microparticles to navigate in three-dimensional space and overcome larger viscous drag forces.

References

[1] J. J. Abbott, Z. Nagy, F. Beyeler, and B. J. Nelson, "Robotics in the small, part I: microbotics," *IEEE Robotics and Automation Magazine*, vol. 14, no. 2, pp. 92-103, June 2007.

[2] L. Dong and B. J. Nelson, "Tutorial-Robotics in the small part II: nanorobotics," *IEEE Robotics and Automation Magazine*, vol. 14, no. 3, pp. 111-121, September 2007.

[3] S. Biller, D. Baumgarten, and J. Haueisen, "A novel marker design for magnetic marker monitoring in the human gastrointestinal tract," *IEEE Transactions on Biomedical Engineering*, vol. 58, no. 12, pp. 3368-3375, December 2011.

[4] W. Weitschies, M. Karaus, D. Cordini, L. Trahms, J. Breitkreutz, and W. Semmler, "Magnetic marker monitoring of disintegrating capsules," *European Journal of Pharmaceutical Sciences*, vol. 13, pp. 411-416, April 2001.

[5] J. J. Abbott, O. Ergeneman, M. P. Kummer, A. M. Hirt, and B. J. Nelson, "Modeling magnetic torque and force for controlled manipulation of soft-magnetic bodies," *IEEE Transactions on Robotics*, vol. 23, no. 6, pp. 1247-1252, December 2007.

[6] M. P. Kummer, J. J. Abbott, B. E. Kartochvil, R. Borer, A. Sengul, and B. J. Nelson, "OctoMag: an electromagnetic system for 5-DOF wireless micromanipulation," *IEEE Transactions on Robotics*, vol. 26, no. 6, pp. 1006-1017, December 2010.

[7] S. Martel, J. B. Mathieu, O. Felfoul, H. Macicior, G. Beaudoin, G. Soulez, and L. H. Yahia, "Adapting MRI systems to propel and guide microdevices in the human blood circulatory system," in *Proceedings of the International Conference of the IEEE Engineering in Medicine and Biology Society (EMBS)*, pp. 1044-1047, San Francisco, USA, September 2004.

[8] J. B. Mathieu, S. Martel, L. H. Yahia, G. Soulez, and G. Beaudoin, "MRI systems as a mean of propulsion for a microdevice in blood vessels," in *Proceedings of the International Conference of the IEEE Engineering in Medicine and Biology Society (EMBS)*, vol. 4, pp. 3419-3422, Montreal, Canada, September. 2003.

[9] R. G. McNeil, R. C. Ritter, B. Wang, M. A. Lawson, G. T. Gillies, K. G. Wika, E. G. Quate, M. A. Howard, and M. S. Grady, "Characteristics of an improved magnetic-implant guidance system," *IEEE Transactions on Biomedical Engineering*, vol. 42, no. 8, pp. 802-808, August 1995.

[10] G. T. Gillies, R. C. Ritter, W. C. Broaddus, M. S. Grady, M. A. Howard, and R. G. McNeil, "Magnetic manipulation instrumentation for medical physics research, "*Review of Scientific Instruments*, vol. 65, no. 3, pp. 533-562, March 1994.

[11] D. C. Meeker, E. H. Maslen, R. C. Ritter, and F. M. Creighton, "Optimal realization of arbitrary forces in a magnetic stereotaxis system," *IEEE Transactions on Magnetics*, vol. 32, no. 2, pp. 320-328, March 1996.

[12] K. Ishiyama, K. I. Arai, M. Sendoh, and A. Yamazaki, "Spiral-type micro-machine for medical applications," in *Proceedings of the IEEE International Symposium of Micromechatronics and Human Science (MHS)*, pp. 65-69, 2000.

[13] S. S. Shevkoplyas, A. C. Siegel, R. M. Westervelt, M. G. Prentiss, and G. M. Whitesides, "The force acting on a superparamagnetic bead due to an applied magnetic field," *Lab on a Chip*, vol. 7, no. 10, pp. 1294-1302, July 2007.

[14] J. D. Keuning, J. de Vries, L. Abelmann, and S. Misra, "Image-based magnetic control of paramagnetic microparticles in water," in *Proceedings of the IEEE International Conference of Robotics and Systems (IROS)*, pp. 421-426, San Francisco, USA, September 2011.

[15] X. Liu and D. Gong, "A comparative study of A-star algorithms for search and rescue in perfect maze," in *Proceedings of the IEEE International Conference on Electric Information and Control Engineering (ICEICE)*, pp. 24-27, Wuhan, China, April 2011.

[16] T. Tsuji, P. G. Morasso, and M. Kaneko, "Trajectory generation for manipulators based on artificial potential field approach with adjustable temporal behavior," in *Proceedings of the IEEE International Conference of Robotics and Systems (IROS)*, vol. 2, pp. 438-443, Osaka, Japan, November 1996.

[17] D. F. Guang, J. Peng, B. X. Qian, and W. H. Jian, "AUV local path planning based on virtual potential field," in *Proceedings of the IEEE International Conference on Mechatronics and Automation (ICMA)*, pp. 1711-1716, Niagara Falls, Canada, May 2005.

[18] R. Daily and D. M. Bevly, "Harmonic potential field path planning for high speed vehicles," in *Proceedings of the American Contntrol Conference (ACC)*, pp. 4609-4614, Washington, USA, June 2008.

[19] F. Carpi and C. Pappone, "Magnetic maneuvering of endoscopic capsules by means of a robotic navigation system," *IEEE Transactions on Biomedical Engineering*, vol. 56, no. 5, pp. 1482-1490, May 2009.

[20] B. D. Cullity and C. D. Graham, "Introduction to magnetic materials,", 2nd ed. *Hoboken, NJ: Wiley*, 2009.

[21] K. B. Yesin, K. Vollmers and B. J. Nelson, "Modeling and control of untethered biomicrorobots in a fluidic environment using electromagnetic fields," *International Journal of Robotics Research*, vol. 28, no. 5-6, pp. 527-536, June 2006.

[22] D. R. Nelson, D. B. Barber, T. W. McLain, and R. W. Beard, "Vector field path following for small unmanned air vehicles," in *Proceedings of the American Control Conference (ACC)*, pp. 5788-5794, Minneapolis, USA, June 2006.